**Fig. 3** Time-lapse observations of the fluorescence of osteoblasts cultured on CpTi and AhTi plates and analysis of nodule formation. **a** Serial low-magnification images of a CpTi plate and an AhTi plate obtained by confocal fluorescence microscopy. *Scale bar* 500 μm. **b** Changes in total fluorescent area on CpTi and AhTi plates. Images were obtained by time-lapse observations of the same sample ($n = 3$). **c** Changes in nodule numbers counted in low-magnification images. **d** Changes in average size of nodules. Data shown in **b–d** are mean ± SD. *$p < 0.05$. **e** Distribution of the size and number of nodules in an individual sample
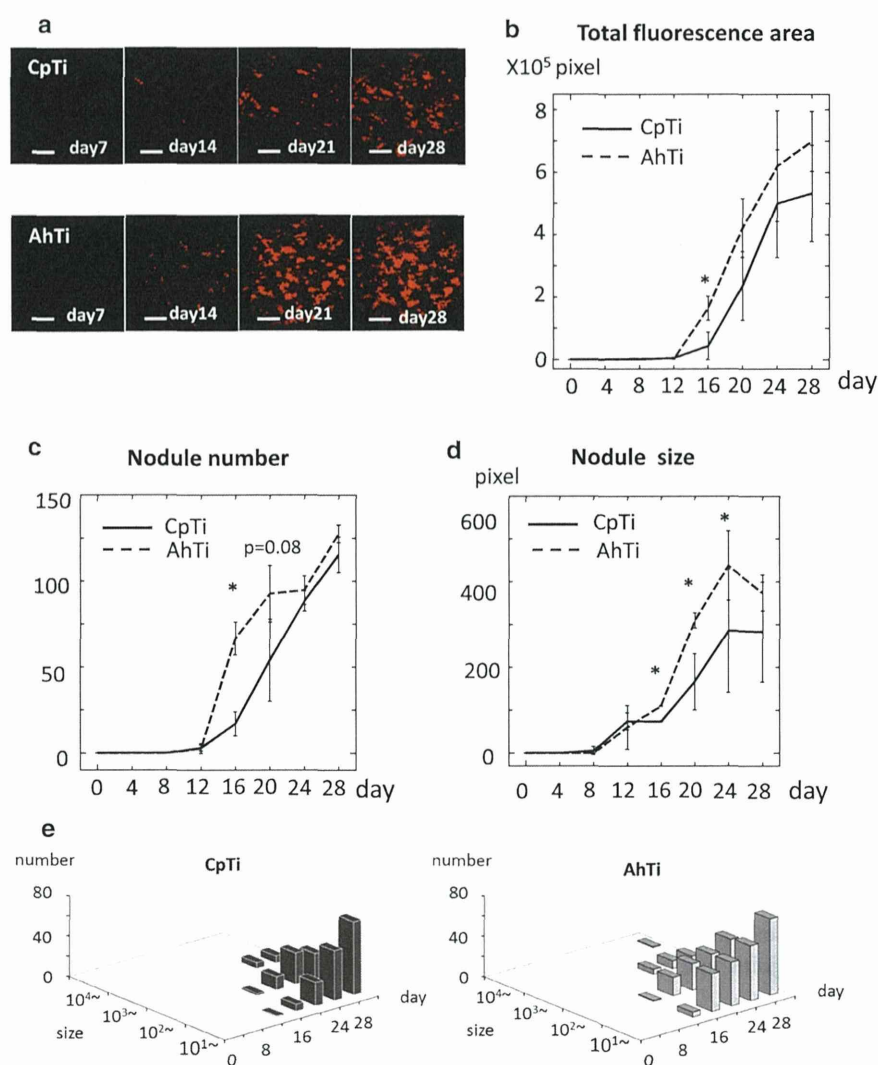
Osteoblasts grown on AhTi plates expressed red fluorescence in a larger area throughout the observation period compared with those grown on CpTi plates

To visualize the time course and spatial distribution of osteoblast proliferation and differentiation on the biomaterials used in this culture system, serial images of the same sample sets were obtained over 4 weeks (Fig. 3a). As shown in Fig. 3b, the fluorescent area began to increase on culture day 16 on both materials. The fluorescent area on day 16 was three times larger on AhTi plates ($1.65 \times 10^5 \pm 3.87 \times 10^4$ pixels) than on CpTi plates ($4.39 \times 10^4 \pm 4.45 \times 10^4$ pixels), and this difference continued throughout the observation period. However, the average daily increase in the total fluorescent area between days 16 and 24 was 5.70×10^4 pixels/day for CpTi plates and 5.68×10^4 pixels/day for AhTi plates, which did not differ between materials.

Multifocal nodule formation was observed on AhTi plates

The nodule numbers counted as fluorescent spots in low-magnification images are shown in Fig. 3c, and the average sizes of these nodules are shown in Fig. 3d. On day 16, the nodule number was three times higher in the AhTi plates (66.7 ± 9.45) than in the CpTi plates (17 ± 6.93) ($p < 0.05$). By contrast, the average nodule size was 1.5 times larger in the AhTi plates (110 ± 1.21) than in the CpTi plates (73.3 ± 061) ($p < 0.05$). To gain an overview of nodule development, the distribution of the sizes and numbers of nodules in a sample is shown in Fig. 3e. There were more small nodules in the AhTi plate throughout the observation period (Table 1). These results indicate that AhTi plates accelerated the onset of differentiation, but once the process had started the progression was less affected by the treatment.
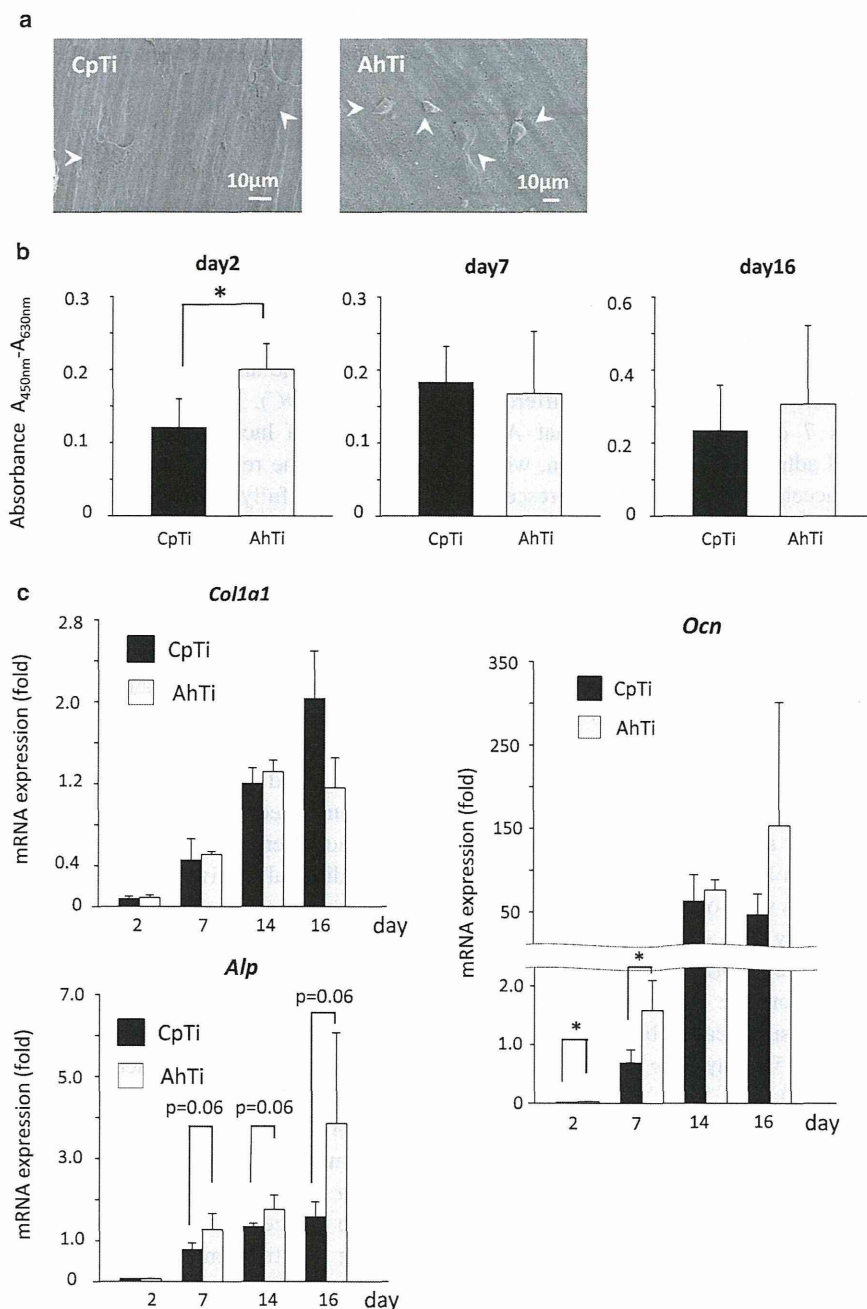
Fig. 4 Evaluation of proliferation and differentiation of osteoblasts cultured on CpTi and AhTi plates using conventional methods. **a** SEM images of osteoblasts cultured on a CpTi or AhTi plate on day 2. *White arrowheads* indicate the cell body. **b** The results of XTT assay on culture days 2, 7, and 16 show greater proliferation of cells grown on AhTi plates compared with those grown on CpTi plates on day 2 ($p < 0.05$). **c** Real-time RT-PCR analysis of *Col1a1*, *Alp*, and *Ocn* expression. Data are presented as mean $\pm$ SD ($n = 4$), *$p < 0.05$. Fold changes are adjusted relative to *GAPDH* expression

SEM observations, XTT assay, and RT-PCR showed increased proliferation and differentiation of osteoblasts on AhTi plates

SEM observations, XTT assays, and RT-PCR analysis were performed to relate the results obtained by fluorescence observations to known indicators of osteoblast proliferation and differentiation. SEM observations on culture day 2 showed favorable attachment of osteoblasts to both materials (Fig. 4a). The morphology of the osteoblasts differed between materials: osteoblasts were large and flat on CpTi plates but small and rounded on AhTi

Table 1 Numbers of nodules smaller than 10^3 pixels

	Day 4	Day 8	Day 12	Day 16	Day 20	Day 24	Day 28
CpTi	0	0	1	7	23	49	72
AhTi	0	0	5	37	43	54	75

plates. These differences in shape reflect differences in the surface characteristics of the materials. The results of the XTT analysis of cell number are shown in Fig. 4b. On day 2, the mean absorbance was 60 % higher for AhTi plates ($0.201 \pm 0.0352/cm^2$) than for CpTi plates ($0.121 \pm 0.0393/cm^2$) ($p < 0.05$). However, no significant difference was observed on days 7 day 16, indicating that AhTi treatment promoted cell adhesion and proliferation, which were related to the accelerated onset of fluorescence expression on AhTi plates.

Osteoblast-specific gene expression levels were determined using RT-PCR on days 2, 7, 14, and 16 (Fig. 4c). *Alp* expression increased throughout the observation period for cells grown on both materials. The cells on AhTi plates had a non-significantly higher *Alp* expression level on day 7 ($p = 0.06$), day 14 ($p = 0.06$), and day 16 ($p = 0.06$) than cells grown on CpTi plates. *Ocn* expression increased on day 14 for both materials. These results are compatible with the finding that the fluorescence expression driven by the *Col1a1* 2.3-kb promoter started increasing around day 16. Although the expression levels were low, significantly higher *Ocn* expression levels were observed on AhTi plates on day 2 ($p < 0.05$) and day 7 ($p < 0.05$) compared with those observed on CpTi plates. *Col1a1* expression for both materials increased throughout the observation period, but its expression did not differ significantly between CpTi and AhTi plates (day 2, $p = 0.51$; day 7, $p = 0.62$; day 14, $p = 0.27$; day 16, $p = 0.79$).

Bone formation around the materials was visualized and quantified in the in vivo system

Next, to assess the application of this system for in vivo evaluation of materials, we quantified the newly formed bone around the intramedullary materials in the fluorescence images. The gross appearance of the operative procedure and an X-ray image of the implanted wire are shown in Fig. 5a, b. Twenty-eight days after implantation, the wires were removed and fluorescence images were obtained (Fig. 5c). The fluorescent area was five times larger for the AhTi wires than the CpTi wires (Fig. 5d). Newly formed bone was also quantified using the affinity indexes obtained from histological sections stained with Van Gieson's picrofuchsin (Fig. 5e). The affinity index was 60 % higher for AhTi wires (46.1 ± 22.9 %) than

CpTi wires (27.9 ± 33.5 %). These results are compatible with the fluorescence observations (Fig. 5f).

Discussion

Several noninvasive bioimaging techniques for visualizing osteoblast differentiation have been reported. Iris et al. [13] reported a bioluminescence imaging method for visualizing differentiation of bone marrow-derived mesenchymal stem cells to osteoblasts in transgenic mice harboring the firefly luciferase gene under the control of the human osteocalcin promoter (*hOC*). They also reported the time course of the expression of luciferase during in vivo skeletal development and bone repair. Expression of the *hOC* promoter is restricted to fully differentiated osteoblasts. However, in the field of material evaluation, a broader range of differentiation stages is preferable for imaging, and bioluminescence imaging is inadequate for obtaining high-resolution images. Kuhn et al. [5] reported a fluorescence imaging system for observing osteoblasts from transgenic mice harboring the *GFP* transgene under the control of the 2.3-kb fragment of the *Col1a1* promoter cultured on carbonated hydroxyapatite-coated disks. In this study, we used mRFP1 instead of GFP because of its greater tissue penetration and spectral separation from autofluorescence and other fluorescent proteins [14], which enabled us to perform additional in vivo evaluation of the materials free of background fluorescence. mRFP1 is a true monomeric variant of the red fluorescent protein DsRed isolated from *Discosoma* sp. In contrast to DsRed, which is known to affect embryonic stem cell development due to its obligate tetramerization [15], the safety of mRFP1 has been well established. Transgenic mice with a ubiquitously high expression of mRFP1 have been reported to show no difference from their non-transgenic littermates in embryonic development, adult organ maturation [16], and neural and muscular functions [17]. The irradiation damage caused by a laser to induce fluorescence may be of concern. However, scanning electron microscopic observation of cochleas stained with fluorescent dyes after laser irradiation using confocal laser microscopy showed no cellular or ultrastructural damage at a normal laser intensity [18]. Therefore, fluorescence imaging using mRFP1 may be a suitable method for the noninvasive imaging of living cells. Another report involved imaging of alkaline phosphatase activity using a fluorinated ALP substrate detected with ^{19}F magnetic resonance spectroscopic imaging after hydrolysis [19]. Although this method is a useful noninvasive method of visualizing osteoblasts, it requires special reagents and analytical equipment.

Formation of a calcified extracellular matrix is an obvious indicator of osteoblast maturation. Quantification

Fig. 5 In vivo evaluation of CpTi and AhTi wires. **a** A sample wire was placed in the right femur of the mouse, the ends of the wire were bent, and the skin was sutured over them. **b** X-ray image of an implanted wire. **c** Fluorescence images of extracted wires were obtained 28 days after implantation. Zoomed images of *white boxed* areas of CpTi and AhTi plates are shown on the *right* of each image. **d** Newly formed bone around the wires was detected as *red spots* and the areas were measured ($n = 4$). AhTi wires showed significantly larger fluorescent areas compared with CpTi wires ($p < 0.05$). **e** Cross-sectional slices of CpTi and AhTi wires implanted for 28 days in mouse femurs. Zoomed images of *yellow boxed* areas are shown on the right. Bone tissue stained *red* with Van Gieson's picrofuchsin is observed on the surface of the AhTi wire but not on the CpTi wire. **f** Affinity indexes of CpTi and AhTi wires ($n = 4$). The affinity index was significantly higher in the AhTi wires than in the CpTi wires ($p < 0.05$). Data are presented as mean ± SD ($n = 4$), *$p < 0.05$
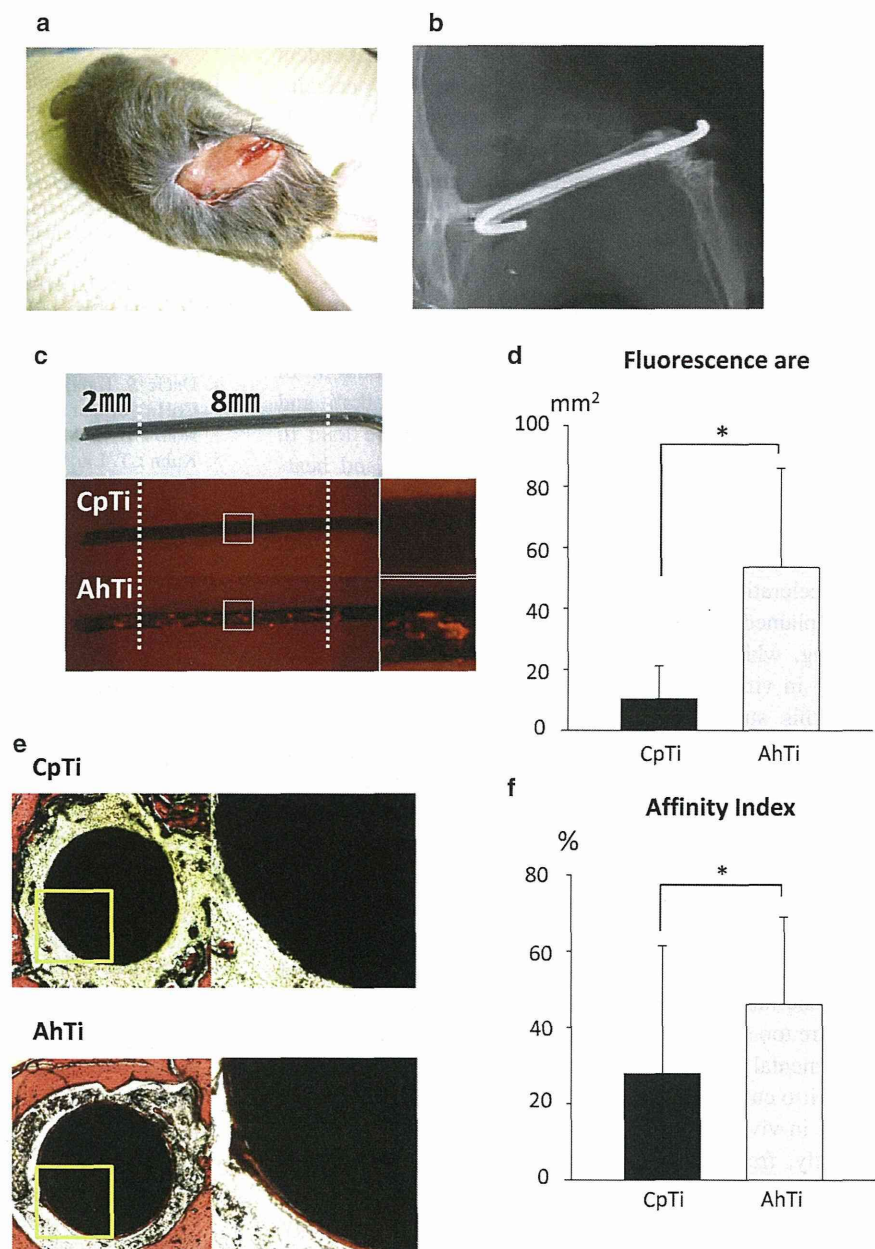
of calcified nodules is often used to evaluate the in vitro bone-bonding ability of biomaterials [20]. Several techniques for detecting nodules or mineral deposition on opaque materials have been reported. They include histological methods (von Kossa or Alizarin Red S staining), fluorescence labeling (tetracycline, calcein blue, etc.) [21, 22], detection of the crystalline structure of calcium phosphate using X-ray diffractometry, Fourier transform infrared spectrometry (FTIR) [23], and scanning electron microscopy [24, 25]. Histological analysis is easy and has been used for decades. However, except for FTIR, none of these techniques can distinguish cell-

mediated calcification from spontaneous precipitation of calcium phosphate in degraded tissues. In this study, the fluorescent substance was produced by transgenic mice, and the fluorescence detected from nodules definitely reflected cell-mediated calcification. Our method may be the first valid method for detecting cell-mediated calcification.

We performed serial observation of the same sample and found that materials with bone-binding ability showed multifocal development of nodules from the time of the initial formation but that the rate of the increase in size of the nodules did not differ between the materials. Maeda

et al. [22] reported their noninvasive observations of nodule formation and quantified the time-dependent increase in green fluorescent emission from calcein-labeled nodules formed by rat mesenchymal stem cells cultured in osteogenic medium supplemented with calcein. However, they did not evaluate the characteristics of individual nodules. Our study is the first to quantify the change in both nodule number and average size with time in cells grown on biomaterials. We found a difference in the pattern of nodule formation between materials according to their bone-bonding ability. AhTi plates had accelerated growth and multifocal nodule formation. In large animal experiments, the application of alkali and heat treatment accelerates the increase in failure load in detaching tests [6]. The failure load of alkali- and heat-treated implants was significantly higher than that of control titanium implants at 4 weeks. Although further studies on other bone-bonding biomaterials are required, the acceleration of an increase in failure load in vivo may be explained by accelerated multifocal bone–material bonding, which is represented as multifocal nodule formation in vitro.

In this study, we also used fluorescence images to quantify new bone formation around the biomaterial in vivo. Compared with conventional histological evaluation, this technique is easy to perform and requires no sample preparation before observation. The bone-bonding ability of biomaterials has not been evaluated in transgenic animals with an introduced fluorescent marker gene. This may be because the genetics of large animals commonly used in biomaterial evaluation have not been well studied and gene-modified animals are not available. Although mice are too small to undergo mechanical tests, our in vivo experimental model is useful for confirming the results of an in vitro culture system and may be a promising modality for the in vivo study of biomaterials.

Lastly, from the point of animal welfare, this system may help reduce the number of animals needed for experimental work. Evaluating the same sample repeatedly would require fewer samples and cells, and hence fewer neonatal mice. Establishment of an osteoblastic cell line from this transgenic mouse could reduce the number of experimental animals needed for research even further.

In conclusion, we performed noninvasive serial observations of osteoblast proliferation, differentiation, and nodule formation on biomaterials. This system may be a promising method for screening and studying the bone-bonding ability of biomaterials.

References

1. Nakamura T, Yamamuro T, Higashi S, Kokubo T, Itoo S (1985) A new glass-ceramic for bone replacement: evaluation of its bonding to bone tissue. J Biomed Mater Res 19:685–698
2. Blum JS, Temenoff JS, Park H, Jansen JA, Mikos AG, Barry MA (2004) Development and characterization of enhanced green fluorescent protein and luciferase expressing cell line for nondestructive evaluation of tissue engineering constructs. Biomaterials 25:5809–5819
3. Xia Z, Ye H, Locklin RM, Ferguson DJ, Cui Z, Triffitt JT (2005) Efficient characterisation of human cell-bioceramic interactions in vitro and in vivo by using enhanced GFP-labelled mesenchymal stem cells. Biomaterials 26:5790–5800
4. Dacic S, Kalajzic I, Visnjic D, Lichtler AC, Rowe DW (2001) Col1a1-driven transgenic markers of osteoblast lineage progression. J Bone Miner Res 16:1228–1236
5. Kuhn LT, Liu Y, Advincula M, Wang YH, Maye P, Goldberg AJ (2010) A nondestructive method for evaluating in vitro osteoblast differentiation on biomaterials using osteoblast-specific fluorescence. Tissue Eng Part C Methods 16:1357–1366
6. Yan WQ, Nakamura T, Kobayashi M, Kim HM, Miyaji F, Kokubo T (1997) Bonding of chemically treated titanium implants to bone. J Biomed Mater Res 37:267–275
7. Kawanabe K, Ise K, Goto K, Akiyama H, Nakamura T, Kaneuji A, Sugimori T, Matsumoto T (2009) A new cementless total hip arthroplasty with bioactive titanium porous-coating by alkaline and heat treatment: average 4.8-year results. J Biomed Mater Res B Appl Biomater 90:476–481
8. Isaac J, Galtayries A, Kizuki T, Kokubo T, Berda A, Sautier JM (2010) Bioengineered titanium surfaces affect the gene-expression and phenotypic response of osteoprogenitor cells derived from mouse calvarial bones. Eur Cell Mater 20:178–196
9. Nishio K, Neo M, Akiyama H, Nishiguchi S, Kim HM, Kokubo T, Nakamura T (2000) The effect of alkali- and heat-treated titanium and apatite-formed titanium on osteoblastic differentiation of bone marrow cells. J Biomed Mater Res 52:652–661
10. Wong GL, Cohn DV (1975) Target cells in bone for parathormone and calcitonin are different: enrichment for each cell type by sequential digestion of mouse calvaria and selective adhesion to polymeric surfaces. Proc Natl Acad Sci USA 72:3167–3171
11. Roehm NW, Rodgers GH, Hatfield SM, Glasebrook AL (1991) An improved colorimetric assay for cell proliferation and viability utilizing the tetrazolium salt XTT. J Immunol Methods 142:257–265
12. Maniatopoulos C, Rodriguez A, Deporter DA, Melcher AH (1986) An improved method for preparing histological sections of metallic implants. Int J Oral Maxillofac Implant Summer 1:31–37
13. Iris B, Zilberman Y, Zeira E, Galun E, Honigman A, Turgeman G, Clemens T, Gazit Z, Gazit D (2003) Molecular imaging of the skeleton: quantitative real-time bioluminescence monitoring gene expression in bone repair and development. J Bone Miner Res 18:570–578
14. Campbell RE, Tour O, Palmer AE, Steinbach PA, Baird GS, Zacharias DA, Tsien RY (2002) A monomeric red fluorescent protein. Proc Natl Acad Sci USA 99:7877–7882
15. Hadjantonakis AK, Macmaster S, Nagy A (2002) Embryonic stem cells and mice expressing different GFP variants for multiple non-invasive reporter usage within a single animal. BMC Biotechnol 2:11
16. Zhu H, Wang G, Li G, Han M, Xu T, Zhuang Y, Wu X (2005) Ubiquitous expression of mRFP1 in transgenic mice. Genesis 42:86–90
17. Long JZ, Lackan CS, Hadjantonakis AK (2005) Genetic and spectrally distinct in vivo imaging: embryonic stem cells and

mice with widespread expression of a monomeric red fluorescent protein. BMC Biotechnol 5:20

18. Flock A, Flock B, Scarfone E (1998) Laser scanning confocal microscopy of the hearing organ: fluorochrome-dependent cellular damage is seen after overexposure. J Neurocytol 27:507–51615

19. Gade TP, Motley MW, Beattie BJ, Bhakta R, Boskey AL, Koutcher JA, Mayer-Kuckuk P (2011) Imaging of alkaline phosphatase activity in bone tissue. PLoS One 6:e22608

20. Declercq HA, Verbeeck RM, De Ridder LI, Schacht EH, Cornelissen MJ (2005) Calcification as an indicator of osteoinductive capacity of biomaterials in osteoblastic cell cultures. Biomaterials 26:4964–4974

21. Goto T, Kajiwara H, Yoshinari M, Fukuhara E, Kobayasi S, Tanaka T (2003) In vitro assay of mineralized-tissue formation on titanium using fluorescent staining with calcein blue. Biomaterials 24:3885–3892

22. Maeda M, Hirose M, Ohgushi H, Kirita T (2007) In vitro mineralization by mesenchymal stem cells cultured on titanium scaffolds. J Biochem 141:729–736

23. Boyan BD, Bonewald LF, Paschalis EP, Lohmann CH, Rosser J, Cochran DL, Dean DD, Schwartz Z, Boskey AL (2002) Osteoblast-mediated mineral deposition in culture is dependent on surface microtopography. Calcif Tissue Int 71:519–529

24. Stanford CM, Jacobson PA, Eanes ED, Lembke LA, Midura RJ (1995) Rapidly forming apatitic mineral in an osteoblastic cell line (UMR 106-01 BSP). J Biol Chem 270:9420–9428

25. Boskey AL (2003) Mineral analysis provides insights into the mechanism of biomineralization. Calcif Tissue Int 72:533–536

The coronal alignment after medial unicompartmental knee arthroplasty can be predicted: usefulness of full-length valgus stress radiography for evaluating correctability

Yasutaka Tashiro · Shuichi Matsuda · Ken Okazaki ·
Hideki Mizu-uchi · Umito Kuwashima · Yukihide Iwamoto

Abstract

Purpose We aimed to clarify whether the coronal alignment after medial unicompartmental knee arthroplasty (UKA) is predictable using preoperative full-length valgus stress radiography.

Methods Thirty-seven consecutive patients with a mean age of 71.5 ± 7.0 years awaiting medial UKA were recruited. Full-length weight-bearing radiographs of the lower limbs were obtained pre- and postoperatively. Preoperative full-length valgus stress radiography in the supine position was also performed, and the transition of the hip-knee-ankle angle (HKAA) and the weight-bearing ratio were assessed. The tibia first cut technique was used, and the distal femur was cut parallel to the cutting surface of the proximal tibia during surgery.

Results The mean postoperative HKAA was $2.0° \pm 2.1°$ varus, and the mean weight-bearing ratio was 43.1 ± 7.7 %; each of these parameters demonstrated significantly strong correlations with the values on the preoperative valgus stress radiographs ($p < 0.01$), while the correlation between the postoperative alignment and the preoperative standing alignment without stress was moderate ($p < 0.01$). The postoperative alignment was slightly undercorrected compared to that observed on the valgus stress radiographs ($p < 0.05$), and no knees exhibited evident overcorrection compared to that on the valgus stress radiographs.

Conclusion Preoperative valgus stress radiography is useful for evaluating the correctability of varus deformities and predicting the postoperative coronal alignment. For clinical relevance, performing preoperative valgus stress radiography would help to more precisely select patients and, when combined with the tibia first cut technique, aid in achieving the expected knee alignment and avoid severe undercorrection or overcorrection.

Level of evidence Diagnostic study, Level II.

Keywords Unicompartmental knee arthroplasty ·
Valgus stress radiography · Tibia first cut technique ·
Correctability · Coronal alignment

Y. Tashiro (✉) · K. Okazaki · H. Mizu-uchi · U. Kuwashima ·
Y. Iwamoto
Department of Orthopaedic Surgery, Graduate School of Medical
Sciences, Kyushu University, 3-1-1 Maidashi, Higashi-ku,
Fukuoka 812-8582, Japan
e-mail: 11yasu@med.kyushu-u.ac.jp

S. Matsuda
Department of Orthopaedic Surgery, Graduate School
of Medicine, Kyoto University, 54 Kawahara-cho,
Shogoin, Sakyo-ku, Kyoto 606-8507, Japan

Introduction

Unicompartmental knee arthroplasty (UKA) relieves pain and restores the knee function in patients with localized osteoarthritis of the knee [5, 9, 27, 33, 34]. It is a less invasive surgery that preserves the cruciate ligaments as well as the contralateral tibiofemoral and patellofemoral compartments. Although excellent results for UKA have been reported [6, 9], there remains variability in failure rates. Varus undercorrection or valgus overcorrection sometimes occur and can lead to a poor surgical outcome [1, 33, 38]. Malposition between the femoral and tibial components increases edge loading at the tibial component and can accelerate tibial polyethylene insert wear [2, 14]. Therefore, it is important to place the implant accurately and restore correct knee alignment to achieve a successful postoperative result.

Proper patient selection and the use of accurate surgical techniques are required to achieve successful outcomes

with UKA [10, 16]. The indications for UKA in patients with osteoarthritis and osteonecrosis of the knee should be carefully selected because overcorrection can lead to disease progression in the contralateral compartment. As excessive release of medial soft tissue causes valgus overcorrection in patients treated with medial UKA, surgeons should avoid this procedure. In our hospital, we determine whether UKA is indicated for a given patient by performing full-length anteroposterior radiography under valgus stress in advance and evaluating if the mechanical axis crosses the tibial plateau between the tibial spines before surgery [12, 19]. Valgus stress radiographs are sometimes used to assess the knee condition in patients with osteoarthritic knees [13], however, few studies have so far evaluated the ability to correct varus deformities in the preoperative planning of the lower limb alignment after medial UKA [18, 24, 36]. We refer to this examination, because valgus stress radiography reflects the maximally corrected knee alignment when the medial soft tissue is not released. Regarding the surgical procedure, we adopt the 'tibia first cut technique' to position the femoral and tibial components in parallel both in knee extension and flexion and achieve an adequate limb alignment.

The purpose of this study was to clarify whether preoperative full-length valgus stress anteroposterior (AP) radiography can be used to predict the postoperative knee alignment in patients treated with medial UKA. The hypothesis of this study was that the alignment parameters on preoperative valgus stress AP radiographs, combined with the tibia first cut technique, would be correlated well with the postoperative alignment and be useful for predicting the postoperative alignment and balancing the knee ligament.

Materials and methods

Thirty-seven consecutive patients with osteoarthritis or osteonecrosis in the medial compartment awaiting UKA, participated in the present study. Eight males and 29 females with a mean age of 71.5 years (range 60–86) were included (Table 1). Twenty-four knees exhibited osteoarthritis (OA) and 13 knees exhibited osteonecrosis. None of the subjects had rheumatoid arthritis (RA). The selection of patients for UKA was generally based on the criteria of Kozinn and Scott [21]. Briefly, the patients were over 60 years old, not overly obese (body mass index <30) and did not perform heavy labor. No pain in the patellofemoral or lateral compartment was observed. Radiographically, the lateral compartment was preserved, and the degree of patellofemoral joint degeneration was moderate. The types of varus deformities in all cases were intraarticular, and no extraarticular deformities were included.

Table 1 The preoperative data

Parameter	
Number of patients	37
Male/female	8/29
Osteoarthritis/osteonecrosis	24/13
Age (years)	71.5 (range 60–86)
Height (cm)	154.0 (range 143.0–173.2)
Weight (kg)	60.3 (range 43.0–77.2)
BMI	25.4 (range 19.6–29.8)
MDA (°)	5.3 (range 2.0–7.8)
HKAA (°)	+6.5 (range 2.3–11.8)
WBR (%)	22.2 (range 3.4–45.8)

Plus (+) indicates the varus angle

MDA Metaphyseal-diaphyseal angle of the proximal tibia, *HKAA* Hip-knee-ankle angle, *WBR* Weight-bearing ratio

The metaphyseal-diaphyseal angles (MDA) were checked [22], and the mean MDA was $5.3° \pm 1.5°$ (range $2.0°–7.8°$ varus), with no knees showing severe tibia vara over $11°$. More than $90°$ and less than $5°$ of flexion contractures were required preoperatively. Knees with cruciate ligament deficiency were excluded. Additionally, we placed the most importance on the preoperative coronal knee alignment under valgus stress. To evaluate the possible correction capability of each knee, a full-length anteroposterior stress radiography examination was performed in the supine position with a 150-N valgus force applied by a Telos arthrometer (Telos, Weiterstadt, Germany). We assessed whether the mechanical axis crossed the tibial plateau between tibial spines before deciding to perform surgical treatment. The joint space in the lateral compartment was also checked on the stress radiographs, and the mean thickness was 4.5 ± 1.1 mm (range 3.0–6.5 mm).

Operation

A slightly medial straight skin incision was made. The medial parapatellar retinaculum was incised, and the capsular incision was extended proximally to the vastus medialis oblique (VMO) insertion. In patients whose VMO ran down to the distal level of the superior pole of the patella, we snipped the VMO 1–2 cm proximally. First, the medial compartment of the proximal tibia was cut perpendicular to the long axis in the coronal alignment using extramedullary cutting guide. The tibial sagittal cutting line (the AP axis of the tibia) was made parallel to the medial wall of the intercondylar notch [17]. Medial release for ligament balancing or realignment was not performed, and only medial osteophytes were removed. Second, the distal femur was cut parallel to the proximal tibia in extension, and the posterior femoral condyle was cut parallel to the proximal tibia in
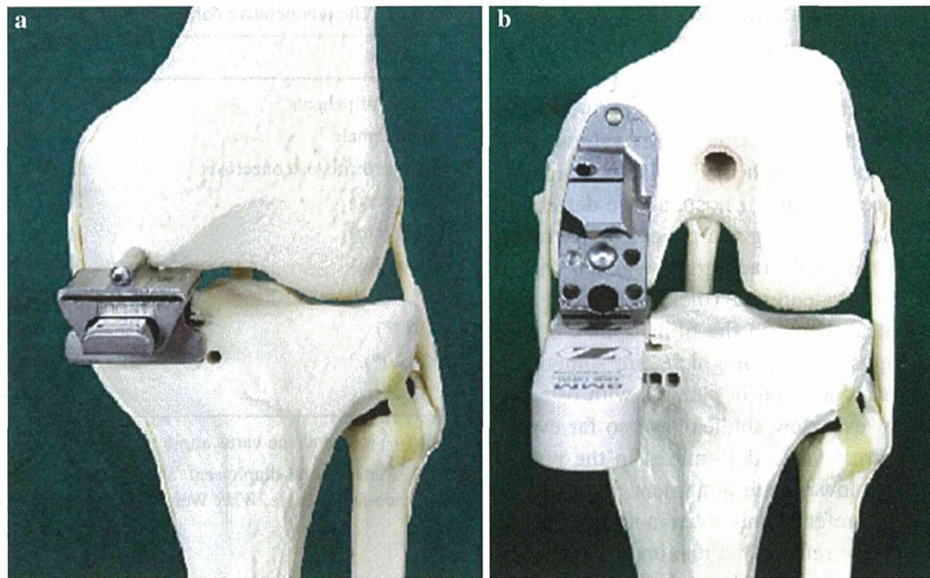
Fig. 1 **a** The distal femur was cut parallel to the cutting surface of the proximal tibia in extension using a metal spacer block. **b** The posterior femoral condyle was cut parallel to the cutting surface of the proximal tibia in flexion using a rectangular gap spacer

flexion using a gap spacer block (Fig. 1a, b). The tibial and femoral components (Zimmer Uni®; Zimmer, Warsaw, IN, USA) were cemented in place. The ligament balance was determined according to the thickness of the polyethylene insert. We used a tension gauge of 2 and 3 mm and chose the thickness of the insert so that the implant gap would be 2 mm.

Evaluation

The coronal alignment of the affected limb was evaluated radiographically. Before surgery, full-length anteroposterior radiographs were obtained in the weight-bearing position. In addition, valgus stress radiography was performed after applying 150-N force to the knee using a Telos arthrometer in the supine position. Postoperatively, full-length weight-bearing anteroposterior radiographs were also obtained 3 weeks after the surgery (Fig. 2a–c). To evaluate the coronal alignment, the hip-knee-ankle angle (HKAA) and the weight-bearing ratio were assessed using the 3D processing software program, Aquarius NET® (TeraRecon, Inc., Foster City, CA). The accuracy of the angle and distance measurement were less than 0.1° and 0.1 mm. HKAA was defined as the angle between the femoral mechanical axis and the tibial mechanical axis [23, 26]. The weight-bearing ratio was calculated by measuring the distance from the medial edge of the proximal tibia to the point where the mechanical axis intersects the proximal tibia, then dividing that measurement by the entire width of the proximal tibia [25]. The presence of edge loading of the femoral component at

the periphery of the tibial insert was surveyed. The occurrence of implant loosening, subsidence, a radiolucent line or progression of osteoarthritis in the lateral compartment was also surveyed at least 6 months postoperatively. The postoperative knee function was clinically evaluated using the Knee Society rating system at the final follow-up [15]. The mean follow-up period was 24.2 (range 6.0–57.8) months. The study protocol was reviewed and approved by the institutional review board of Kyushu University (the approval ID: 25-120), and all patients provided their informed consent before being included in the study.

Statistical analysis

To compare the mean values of the HKAA during preoperative standing, valgus stress in the supine position and postoperative standing radiographs, we used a one-way factorial ANOVA. Fisher's post hoc test was used to compare the mean of one group with the mean of another. The mean values of the weight-bearing ratio under the three conditions were compared in the same way. The relationships between the postoperative alignment values and preoperative alignment values obtained with and without valgus stress were evaluated using Pearson's correlation coefficient to assess whether each parameter could be used to predict the postoperative knee alignment. A p value of 0.05 or less was considered to indicate a significant difference. Power analyses were performed from our sample data on ANOVA (group number = 3, effect size = 0.5, significant level = 0.05, and power = 0.80) and on correlations
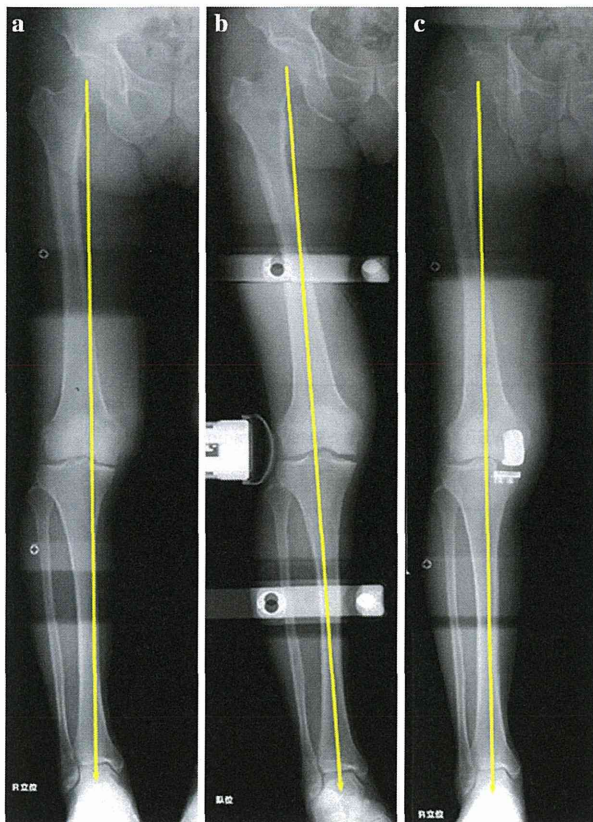
Fig. 2 a A full-length preoperative standing radiograph of an osteonecrosis patient. The *arrow* indicates the mechanical axis. **b** A preoperative valgus stress radiograph obtained in the supine position. A valgus force was applied at 150-N by a Telos arthrometer. **c** A postoperative standing radiograph obtained after medial UKA. The mechanical axis was slightly shifted medially from that observed on the valgus stress radiograph and passed slightly medially to the center of the knee

($r = 0.5$, significant level $= 0.05$, and power $= 0.80$) to indicate sample sizes of 13.9 on ANOVA and 28.9 on correlations could address the questions.

To examine the reproducibility of this method, we randomly selected 10 knees. In these knees, all measurements were repeated three times on three different days by two observers (Y.T. and U.K.) who were blinded to the results

recorded by the other observer, and the intraclass/interclass correlation coefficients (ICCs) were assessed [31]. A repeated one-factor ANOVA was performed to calculate the intraobserver reliability [ICC (1.3)] of the data recorded for the three measurements. The interobserver reliability [ICC (2.3)] was calculated using an unrepeated two-factor ANOVA of the averages of the three measurements obtained by each of the two observers. The reliability of values obtained in the measurements ranged from good to great: the ICC (1.3) values were 0.95 and 0.99 and the ICC (2.3) values were 0.87 and 0.95 for the HKAA and weight-bearing ratio, respectively. The JMP® 9 software program (SAS Institute Inc., Cary, NC, USA) was used for the statistical analysis.

Results

The mean preoperative HKAA on weight-bearing radiographs was 6.5° ± 2.8° varus, corrected to 0.2° ± 2.6° varus with valgus stress ($p < 0.01$). The mean postoperative HKAA on weight-bearing radiographs was 2.0° ± 2.1° varus, which was approximately 2° back to varus alignment than that observed on the preoperative valgus stress radiographs ($p < 0.05$). The mean preoperative weight-bearing ratio on standing radiographs was 22.2 ± 11.0 %, which increased to 48.1 ± 9.4 % with valgus stress ($p < 0.01$). The mean postoperative weight-bearing ratio was 43.1 ± 7.7 %, and the mechanical axis was slightly shifted back to the medial side compared to that observed under preoperative valgus stress ($p < 0.05$) (Table 2). None of the affected knees were overcorrected more than 2° valgus or 5 % lateral postoperatively compared to that observed on the valgus stressed radiographs. The correlations between the full-length weight-bearing alignment before and after the surgery were moderate for both the HKAA ($r = 0.54$, $p < 0.01$) and weight-bearing ratio ($r = 0.47$, $p < 0.01$) measurements (Fig. 3a, b). The alignment values in the preoperative valgus stress radiographs demonstrated a strong correlation with those observed in the postoperative knees for both HKAA ($r = 0.71$, $p < 0.01$) and weight-bearing ratio ($r = 0.64$, $p < 0.01$) (Fig. 3c, d).

Table 2 Transition of the lower limb alignment values on full-length radiography

Parameter	Preoperative standing radiography	Valgus stress radiography	Postoperative standing radiography
HKAA (°)	+6.5 ± 2.8	+0.2 ± 2.6*	+2.0 ± 2.1*,**
WBR (%)	22.2 ± 11.0	48.1 ± 9.4*	43.1 ± 7.7*,**

The values are presented as the mean ± standard deviation. The plus sign indicates the varus angle. The minus sign indicates the valgus angle

HKAA Hip-knee-ankle angle, *WBR* Weight-bearing ratio

* $p < 0.01$ compared with preoperative standing radiography

** $p < 0.05$ compared with preoperative valgus stress radiography